Chaotic motion of localized structures

A. J. Alvarez-Socorro,[1,2] Marcel G. Clerc,[1] Michel Ferré,[1] and Edgar Knobloch[3]
[1]*Departamento de Física and Millennium Institute for Research in Optics, Facultad de Ciencias Físicas y Matemáticas, Universidad de Chile, Casilla 487-3, Santiago, Chile*
[2]*Laboratorio de Investigación, Desarrollo e Innovación, Zenta Group, Diagonal Oriente 5081, Ñuñoa, Santiago, Chile*
[3]*Department of Physics, University of California at Berkeley, Berkeley, California 94720, USA*

(Received 19 November 2019; revised manuscript received 12 January 2020; accepted 23 March 2020; published 27 April 2020)

Mobility properties of spatially localized structures arising from chaotic but deterministic forcing of the bistable Swift-Hohenberg equation are studied and compared with the corresponding results when the chaotic forcing is replaced by white noise. Short structures are shown to possess greater mobility, resulting in larger root-mean-square speeds but shorter displacements than longer structures. Averaged over realizations, the displacement of the structure is ballistic at short times but diffusive at larger times. Similar results hold in two spatial dimensions. The effects of chaotic forcing on the stability of these structures is also quantified. Shorter structures are found to be more fragile than longer ones, and their stability region can be displaced outside the pinning region for constant forcing. Outside the stability region the deterministic fluctuations lead either to the destruction of the structure or to its gradual growth.

DOI: 10.1103/PhysRevE.101.042212

I. INTRODUCTION

A fundamental problem of statistical mechanics is to describe the effect of microscopic scales on macroscopic variables. Usually this effect is modeled in terms of stochastic fluctuations, due to the large number of microscopic degrees of freedom. However, in cases where the number of degrees of freedom is restricted, the fluctuations cannot be taken as stochastic, and in this case their deterministic or chaotic character may play an important role. Here we investigate the effects of the resulting deterministic fluctuations on spatially localized structures (LSs). Such structures are a characteristic feature of self-organized nonequilibrium systems [1–3] and have been observed in numerous fields, ranging from physics and chemistry to engineering and biology. These particlelike states are characterized by continuous order parameters, such as position, width, and amplitude whose evolution may be described by macroscopic equations. The texts [4–6], together with the references cited therein, provide a helpful overview of the subject. In one spatial dimension, the profile of a stationary LS embedded in a featureless background can be interpreted in terms of a spatial trajectory that connects a homogeneous state with itself, i.e., as a homoclinic orbit of a dynamical system evolving in space [7]. In many cases the resulting states may be thought of as bound states of a pair of fronts, one connecting a homogeneous state to a pattern state, while the second connects the pattern state back to the homogeneous state. This is the case, for example, for LSs present in the region of bistability between a homogeneous state and a spatially extended pattern. Such regions typically contain a pinning or snaking interval within which one finds multiple LSs of different lengths organized in a snakes-and-ladders bifurcation diagram [8,9]. The resulting diagram captures the linear stability properties of the LSs as well as their relative (or energy) stability [10].

Localized structures are not necessarily motionless. The motion and complex dynamics of LSs can be the result of a spontaneous symmetry-breaking instability [11–18] or the result of a fluctuating background [19–21]. Despite the ability of existing theory to provide an intuitive picture of the origin of LSs current understanding does not apply to the latter situation. As is well established, additive white noise induces random motion of LSs but ultimately leads to their destruction [22,23]. This is not the case when the forcing is chaotic, i.e., deterministic [24].

Figure 1 illustrates the dramatic difference between deterministic and stochastic forcing of a one-bump LS described by the bistable Swift-Hohenberg equation. In the absence of forcing [Fig. 1(a)] the structure is stable and motionless. With deterministic but chaotic forcing the structure remains stable but executes lateral motion resembling a random walk [Fig. 1(b)], in stark contrast to the effect of multiplicative white noise forcing that ultimately always destroys the structure [Fig. 1(c)]. As discussed further below, this is a consequence of the fact that white noise ultimately explores a wide range of fluctuations, resulting in a potential *noise-induced transition* [25], while those arising from a deterministic origin are bounded by the size of the attractor. In the following we refer to the trajectory in Fig. 1(b) as a *chaotic walk* to distinguish it from the more commonly studied random walk.

The work that follows is motivated by the striking difference between Figs. 1(b) and 1(c). We begin by describing the model problem we study followed by a description of our simulation results in one spatial dimension together with a semi-analytical understanding of the LS mobility characteristics revealed by these simulations as the forcing amplitude increases. The paper concludes with a brief discussion of the two-dimensional case.

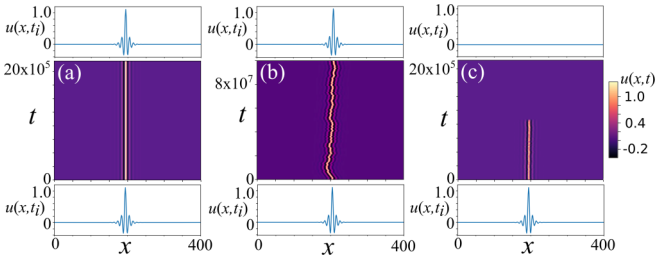

FIG. 1. Spatiotemporal evolution of a one-bump localized solution of the Swift-Hohenberg equation (1) subject to spatiotemporally chaotic forcing with $\mu = 3$ when $\rho = -0.27$, $b = 1.8$ and (a) $\gamma = \eta = 0$, (b) $\gamma = 0.017$, $\eta = 0$, and (c) $\gamma = 0$, $\eta = 5$. The lower and upper panels show the solution profiles at the initial and final times, respectively. Note the much longer timescale in panel (b).

II. THE MODEL

To study the effect of deterministic fluctuations on the dynamics of localized structures, we employ a system of partial differential equations (PDEs) composed of a bistable Swift-Hohenberg (SH) equation subject to multiplicative forcing provided by the Kuramoto-Sivashinsky (KS) equation [24], as described by

$$\partial_t u = \rho u - (1 + \partial_{xx})^2 u + bu^2 - u^3 + \gamma \partial_x \psi(x,t) u + \sqrt{\eta}\zeta(x,t)u, \quad (1)$$

together with

$$\partial_t \psi = -\mu \partial_{xx}\psi - (\partial_x \psi)^2 - \partial_{xxxx}\psi. \quad (2)$$

Here $\zeta(x,t)$ is a Gaussian white noise with zero mean, $\langle \zeta(x,t)\rangle = 0$, and correlation $\langle \zeta(x,t)\zeta(x',t')\rangle = \delta(t-t')\delta(x-x')$ and η represents its intensity, while γ specifies the strength of the multiplicative spatiotemporally chaotic fluctuations experienced by the LSs in Eq. (1) which can be tuned by selecting appropriate values of the parameter μ in Eq. (2) [24]. When $\gamma = \eta = 0$ the system reduces to the usual bistable Swift-Hohenberg equation, whose properties are now well-established [9,26]. Figure 1 shows sample results for $b = 1.8$ and (a) $\gamma = \eta = 0$, (b) $\gamma = 0.017$, $\eta = 0$, i.e., for deterministic forcing. In contrast, Fig. 1(c) is computed from Eq. (1) with stochastic forcing only ($\gamma = 0$).

To investigate the effect of spatiotemporally chaotic fluctuations on the behavior of LSs, we have conducted a numerical study of the model Eqs. (1) and (2) with $\gamma > 0$, $\eta = 0$, and μ sufficiently large that Eq. (2) possesses solutions in the form of spatiotemporal chaos [27]. For the sake of simplicity, periodic boundary conditions are used. Integration was implemented using a fourth-order Runge-Kutta scheme in time with step size $dt = 0.01$ and a finite difference scheme in space that uses a centered stencil of seven grid points. Space was discretized into 400 points with grid size $dx = 0.6$. A stable localized one-bump solution of the bistable Swift-Hohenberg equation ($\gamma = 0$, $\eta = 0$) at $b = 1.8$ and $\rho = -0.27$ was taken as initial condition, motivated by the parameter regime studied in Ref. [9]. This solution can be seen in Fig. 1(a).

The spatiotemporal forcing is provided by the Kuramoto-Sivashinsky equation [28,29], whose dynamics are well explored. In particular, it is known that for $\mu = 3$ this equation

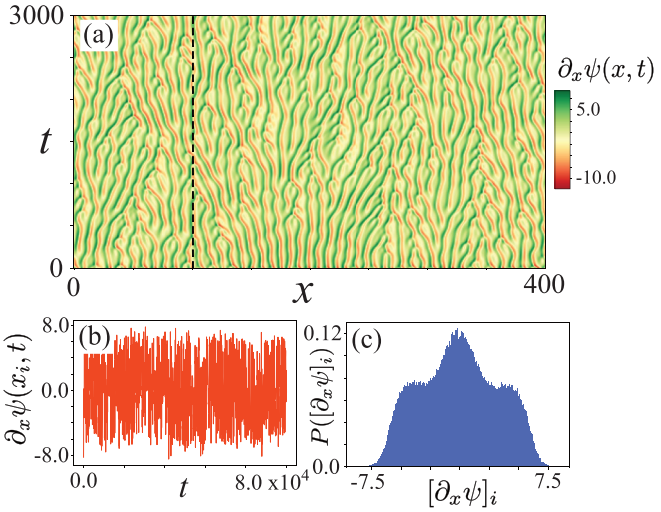

FIG. 2. (a) Spatiotemporal complexity in the Kuramoto-Sivashinsky Eq. (2) at $\mu = 3$. (b) Temporal profile of the fluctuations at the fixed location $x = 100$ [vertical dashed line in (a)] and (c) its probability density function, both at $\mu = 3$.

exhibits spatiotemporally chaotic behavior. Figure 2(a) shows the spatiotemporal chaos at this value of μ while Figs. 2(b) and 2(c) show the resulting forcing amplitude at an arbitrarily selected location $x = 100$ and its probability density function (pdf). It is noteworthy that this density is symmetric with mean zero. Note also that the density has a finite support since the KS attractor is bounded. This is in contrast to white noise.

In the following we employ the parameter values $b = 1.8$ and $\mu = 3$ and vary the parameters ρ, γ while keeping $\eta = 0$ (deterministic forcing). We then compare the results with those for pure stochastic forcing ($\gamma = 0$, $\eta \neq 0$).

III. RESULTS

We now study the effects of the deterministic fluctuations quantified in Section II on the dynamics of the one-bump localized state shown in Fig. 1(a). Figure 3(a) shows the snakes-and-ladders structure of the pinning region when $\gamma = 0$ (blue curves) within the region of bistability between the homogeneous state $u = 0$ (red horizontal line) and the periodic state with 2π wavelength (red curve), both for $b = 1.8$; solid (dashed) lines indicate stable (unstable) states. In the following we call the three lowest stable states LS1, LS2, and LS3, the integer indicating the number of fully developed peaks within the structure. Thus, Fig. 1(a) shows LS1. Superposed on the LS curves are the LS1, LS2, and LS3 states that were found to persist for $t = 10^7$ for three different values of γ and color-coded as follows: $\gamma = 0.006$ (thick red), $\gamma = 0.008$ (thick blue), and $\gamma = 0.015$ (thick yellow), suggesting that in each of these cases these states are in fact stable, albeit in a reduced parameter range: the figure indicates that as the fluctuation amplitude γ increases the snaking zone gradually shrinks but does not disappear. Figures 3(b) and 3(c) portray the surviving snaking zones for $\gamma = 0.006$ and $\gamma = 0.008$, respectively. These results are presented in a different way in Fig. 4 which shows the regions of stable LS1, LS2, and LS3 in the (ρ, γ) plane. Note that as

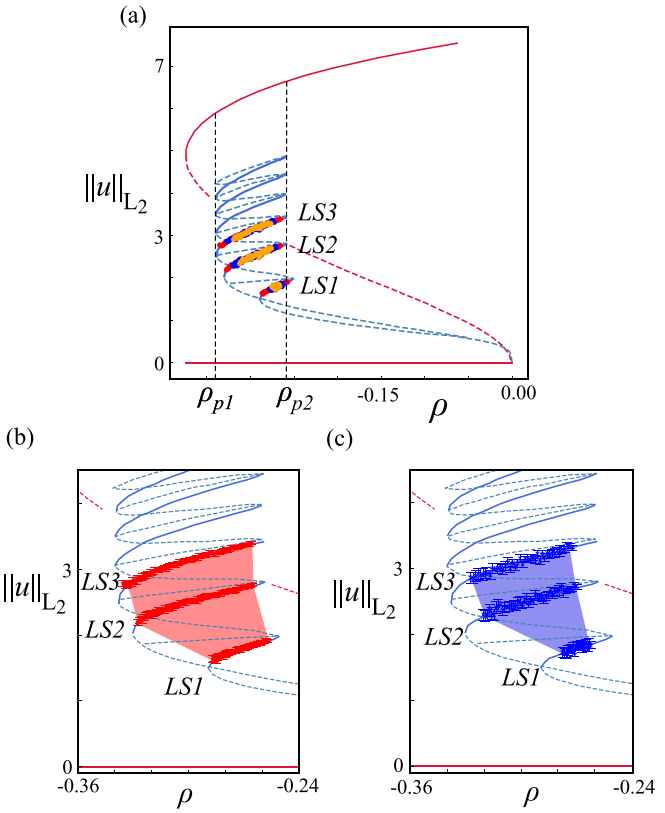

FIG. 3. (a) Snakes-and-ladders structure of the pinning zone when $b = 1.8$ and $\gamma = \eta = 0$ (blue curves) straddling the Maxwell point located at $\rho_M \approx -0.3137$, with superposed stable localized states: $\gamma = 0.006$ (red), $\gamma = 0.008$ (blue), and $\gamma = 0.015$ (yellow), showing the progressive shrinking of the snaking region as γ increases. Dashed lines at ρ_{p1} and ρ_{p2} indicate the width of the pinning zone when $\gamma = \eta = 0$. The corresponding results for (b) $\gamma = 0.006$ and (c) $\gamma = 0.008$ showing, from bottom to top, the branches of stable LS1, LS2, and LS3 as determined from simulations over a time interval $t = 10^7$. In each case the error bars indicate the size of the fluctuations over this timescale.

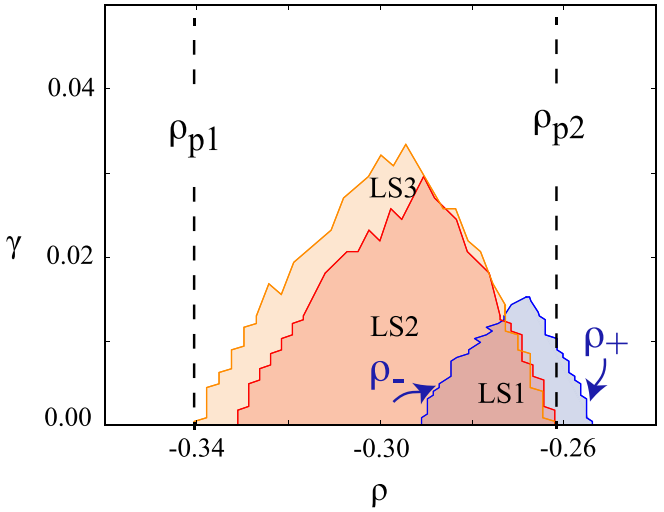

FIG. 4. Regions of stability of LS1, LS2, and LS3 in the (ρ, γ) plane showing that the stability regions become increasingly asymmetrical and in each case close off [at $\gamma = \gamma_c(n)$] when the forcing amplitude γ becomes too large. Dashed lines at ρ_{p1} and ρ_{p2} indicate the width of the pinning zone when $\gamma = \eta = 0$.

γ increases the LSs are eroded more rapidly in the vicinity of the left boundary $\rho = \rho_-(\gamma)$ than near the right boundary $\rho = \rho_+(\gamma)$. This asymmetry arises because the fluctuations near ρ_-, i.e., for values of ρ below the (effective) Maxwell point, favor the homogeneous state, leading to front retraction, while those near ρ_+, i.e., for ρ above the Maxwell point, favor the periodic state and hence front advance. As a result the fluctuations gradually shift the pinning region toward larger values of ρ relative to the case $\gamma = \eta = 0$. We also see that this effect is larger for LSn with small n, and that stable LSn with larger n survive to larger values of γ. As discussed further below this appears to be a consequence of the reduced mobility of larger structures. Figure 5 sheds additional light on this behavior. The left panels show the boundary of the pinning or snaking zone as γ increases across $\gamma_-(\rho)$ [Fig. 5(a)] and across $\gamma_+(\rho)$ [Fig. 5(c)]. Thus, for $\gamma > \gamma_-(\rho)$ the preferred state is $u = 0$ while the opposite is the case for $\gamma > \gamma_+(\rho)$. These observations are reflected in Figs. 5(b) and 5(d) which show that below the pinning region the structure collapses to $u = 0$ [Fig. 5(b)] while above it it gradually nucleates additional wavelengths and so grows in spatial extent [Fig. 5(d)]. Figures 5(a) and 5(c) also show that the lifetime of the localized structures outside their stability region (see Fig. 4) increases rapidly as one approaches the top boundary of the pinning region in the (ρ, γ) plane. We expect that this lifetime increases inversely as the square root of the distance from the boundary of the stability zone much as occurs when $\gamma = 0$ [9].

To explain some aspects of the above results, and in particular the lateral motion of the LSs computed from the PDE system Eqs. (1) and (2), we employ a semianalytical approach, putting the system into the instantaneous comoving frame $z = x - \int_0^t c(t')\,dt'$. Thus, $c(t)$ is the instantaneous velocity

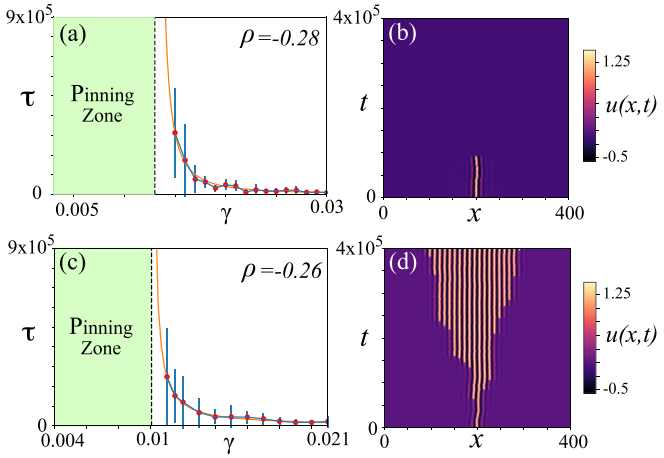

FIG. 5. Lifetimes τ of localized states as a function of γ for $b = 1.8$ and (a) $\rho = -0.28$, (c) $\rho = -0.26$ outside the pinning zone (red dots with error bars). The solid lines represent the fits (a) $\tau = 14.39/(\gamma - 0.013)^{1.6}$, (c) $\tau = 125.9/(\gamma - 0.01)^{1.1}$. (b) Eventual decay of LS1 at $\rho = -0.28$ when $\gamma = 0.0225 > \gamma_-(\rho)$. (d) Gradual growth of LS1 at $\rho = -0.26$ when $\gamma = 0.012 > \gamma_+(\rho)$.

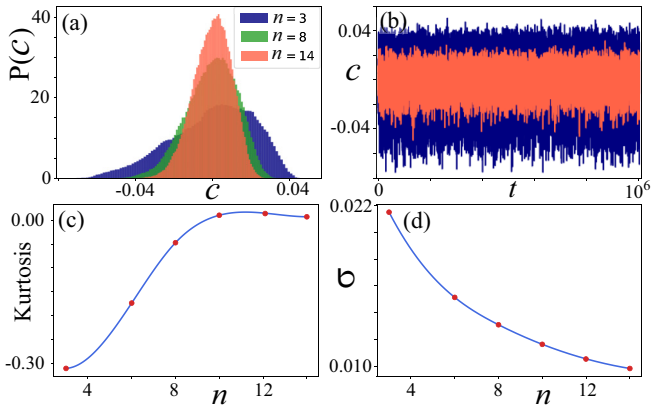

FIG. 6. Characterization of the instantaneous speed $c(t)$ of localized structures as a function of their length n as obtained from Eq. (6) with $b = 1.8$, $\rho = -0.3$, $\gamma = 0.25$, $\eta = 0$, and $\mu = 3$. (a) Probability density function of $c(t)$ for three different values of n. (b) Typical temporal evolution of $c(t)$ for $n = 3$ (dark blue curve) and $n = 14$ (light red curve). The remaining panels show (c) the kurtosis and (d) the standard deviation σ of the pdf of c as functions of n.

of the structure. To simplify the calculation that follows, we use standard bracket notation for the inner product with

$$\langle f \,|\, g \rangle = \int_{-\infty}^{\infty} f(x) g(x)\, dx. \tag{3}$$

We suppose that $|u\rangle = |u_0\rangle + |w\rangle$, where $u_0 \equiv u_0(z)$ is an appropriate LS solution and w is a small perturbation comparable in magnitude to both γ and the instantaneous velocity $c(t)$. It follows that

$$-c\partial_z u_0 = \mathcal{L}\,|w\rangle + \gamma\,|(\partial_z \psi) u_0\rangle\,, \tag{4}$$

where $\mathcal{L} \equiv \rho - (1 + \partial_{zz})^2 + 2\beta u_0 - 3u_0^2$. Since $\mathcal{L}$ is a self-adjoint linear operator (i.e., $\mathcal{L} = \mathcal{L}^\dagger$) with a kernel spanned by $\partial_z u_0$ the solvability condition for $w(x,t)$ yields

$$\dot{x}_c(t) \equiv c(t) = -\gamma \frac{\langle \partial_z u_0 |\, (\partial_z \psi) u_0 \rangle}{\langle \partial_z u_0 |\, \partial_z u_0 \rangle}. \tag{5}$$

Since the structure is localized, integration by parts shows that

$$\dot{x}_c(t) = \gamma \frac{\langle \partial_z u_0 |\, \psi\, \partial_z u_0 \rangle}{\langle \partial_z u_0 |\, \partial_z u_0 \rangle}. \tag{6}$$

This equation governs the motion of the centroid, hereafter $x_c(t)$, of the localized structure and shows that motion results from the asymmetry in the projection of $\psi(z,t)$ on the translation mode $\partial_z u_0(z)$. For fluctuations driven by noise alone we have

$$\dot{x}_c(t) = -\sqrt{\eta} \frac{\langle \partial_z u_0 |\, \zeta(z,t) u_0 \rangle}{\langle \partial_z u_0 |\, \partial_z u_0 \rangle} \equiv \sqrt{\eta}\xi(t), \tag{7}$$

where $\xi(t)$ is a white noise satisfying

$$\langle \xi(t)\xi(t') \rangle_\zeta = \frac{\langle (\partial_z u_0)^2 |\, u_0^2 \rangle}{(\langle \partial_z u_0 |\, \partial_z u_0 \rangle)^2} \delta(t - t'). \tag{8}$$

Figure 6(a) compares the probability density functions of $c(t)$ for localized structures with $n = 3$, 8, and 14, while Fig. 6(b) shows the corresponding realizations $c(t)$ for $n = 3$ and 14. We see that the distribution of speeds is much broader

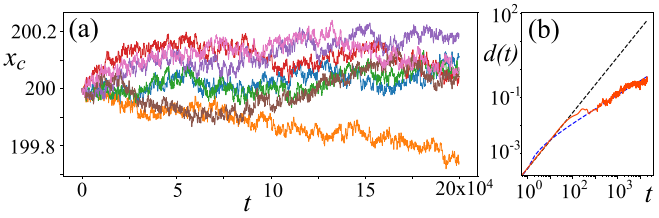

FIG. 7. (a) Position of the centroid $x_c(t)$ for several slightly different one-bump initial conditions when $\rho = -0.27$, $\gamma = 0.001$, $\eta = 0$. (b) Corresponding ensemble-averaged centroid displacement $d(t)$ (red curve). The black-dashed line corresponds to the linear fit $d(t) = 3 \times 10^{-4} t$ to the short-time evolution ($0 \leqslant t \leqslant 100$), while the blue-dashed curve represents the square root fit $d(t) = 0.0013\sqrt{t} - 0.001$ to the subsequent evolution.

when n is small than when it is large, and conclude that narrower structures have greater mobility, a conclusion in agreement with related work on colliding LS [30]. We ascribe this effect to the requirement that to move a broader structure one requires a fluctuation with a larger spatial correlation, making larger speeds less likely. Notice also that the distribution function for small n is markedly asymmetric. This is due to the asymmetry in the forcing function $\partial_x \psi$ with respect to spatial reflection $x \to -x$. Inevitably the resulting asymmetry in the pdf of the speed c decreases with increasing length n of the structure. These properties are summarized in Figs. 6(c) and 6(d) which show the kurtosis of the pdf and its standard deviation σ as a function of n.

IV. STATISTICAL CHARACTERIZATION OF LS DISPLACEMENT

To characterize the dynamics of an LS, we fix attention on its centroid, defined by

$$x_c(t) = \frac{\int_{-L}^{L} x u(x,t)\, dx}{\int_{-L}^{L} u(x,t)\, dx}, \tag{9}$$

where $[-L, L]$ is the domain size. Figure 7 shows the location of this centroid for LS1 as a function of the elapsed time t as determined from numerical simulations of the system Eqs. (1) and (2) starting from several slightly different initial conditions (color-coded) obtained by multiplying u and ψ at the same grid points as the solution by independent random vectors of magnitude 10^{-5}. The results evidence the extreme sensitivity of the drift dynamics to initial conditions, as is expected of a chaotic system.

From the dynamics of the centroid, we can extract its displacement $\Delta x(t) \equiv x_c(t + dt) - x_c(t)$ in time dt for each realization of the chaotic process. Figure 8(a) shows this displacement for one such realization. We see that successive displacements may be considered to be uncorrelated, with zero mean. Indeed, the resulting distribution of Δx resembles a Gaussian distribution [Fig. 8(b)], as may be expected of Brownian motion. However, in the present case the distribution is truncated since very large displacements in the time dt are prohibited. This is a consequence of the fact that the displacement is fully deterministic, with each realization drawn from a bounded attractor. Figure 8(c) shows the expected rapid

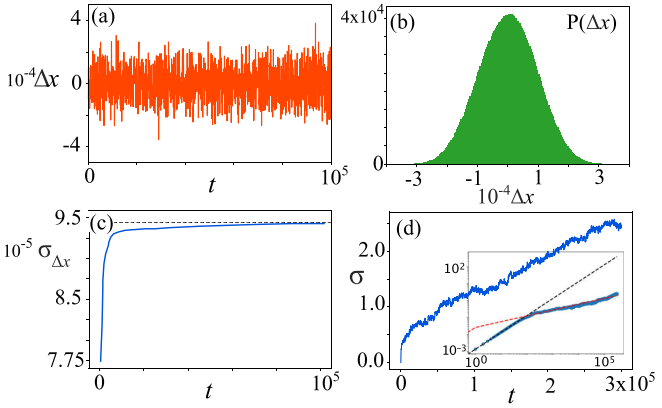

FIG. 8. (a) Displacement Δx of the centroid of a one-bump state as a function of time t in a single realization of the chaotic walk at $\rho = -0.27$ and $\gamma = 0.001$. (b) Associated probability density function $P(\Delta x)$. (c) Evolution of the standard deviation $\sigma_{\Delta x}$ of the resulting displacement dynamics. (d) Ensemble standard deviation $\sigma(t)$ computed over 100 slightly different initial conditions differing by order 10^{-4}. The inset presents the same results on a log-log scale. Initially, a ballistic behavior is observed (exponent 1, $t < 100$, dashed black curve), followed by a crossover to subdiffusive behavior (exponent 0.345, $t > 100$, dashed red curve).

saturation of the standard deviation $\sigma_{\Delta x}(t)$ of Δx. In contrast, Fig. 8(d) shows the cumulative effect of these displacements, i.e., the standard deviation $\sigma(t)$ of the centroid position $x_c(t)$ computed over 100 realizations of the above process, each generated by a small $[O(10^{-4})]$ random perturbation of the initial condition.

Figure 9 shows the corresponding evolution of 3-bump and 14-bump localized states in a space-time diagram. We see that the broader structure has a broader probability distribution function than the shorter structure [Fig. 9(c)]. At first sight this conclusion is in conflict with our mobility calculation. We understand this unexpected result as follows: because broader structures have lower mobility and therefore larger effective inertia, a broader structure, once in motion, will

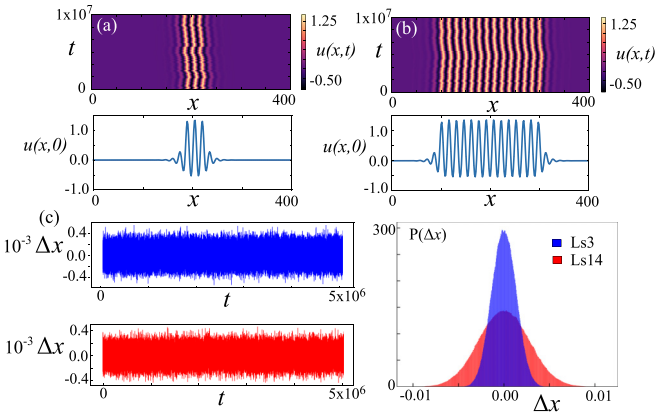

FIG. 9. Space-time evolution of (a) 3-bump and (b) 14-bump localized states when $\rho = -0.28$, $\gamma = 0.012$ showing that the amplitude of the centroid displacement decreases with increasing number of bumps. (c) Displacement Δx of the structures as a function of time together with their pdf.

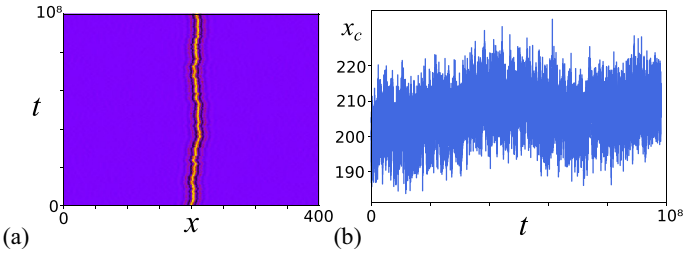

FIG. 10. (a) Spatiotemporal evolution of a one-bump localized solution of the Swift-Hohenberg equation (1) with $b = 1.8$, $\rho = -0.27$, $\eta = 0$ in the presence of additive deterministic fluctuations $\gamma \partial_x \psi(x,t)$ with $\gamma = 0.004$ and $\mu = 3$. (b) Temporal evolution of the centroid position $x_c(t)$.

drift further before it can change direction, resulting in larger typical displacement than for shorter structures.

V. CONCLUSIONS

Based on a prototype model of pattern formation, the Swift-Hohenberg equation, we have shown that localized structures are robust in the presence of multiplicative deterministic fluctuations. This is in contrast to the effect of random fluctuations, which ultimately always destroy such structures. We have seen that in the former case the LSs exhibit complex spatiotemporal behavior we have termed a chaotic walk. This type of walk is highly sensitive to the initial conditions but its properties can nonetheless be described using standard statistical physics approaches including the computation of probability distribution functions. The exploding dissipative solitons studied in Ref. [31] provide a distinct example of a system exhibiting related behavior, where translation is triggered by loss of reflection symmetry. However, in contrast to the system studied here, in this system translation is intermittent and associated with episodic escapes from a reflection-invariant strange attractor as described in Ref. [32]. The resulting walk is thus a chaotic Lévy flight. In contrast our system Eqs. (1) and (2) has no reflection symmetry. As shown in Fig. 10 similar results hold in the case of additive deterministic fluctuations as well.

We have seen that the presence of deterministic fluctuations with increasing amplitude leads to the gradual erosion of the stability zone of different LSs, with shorter structures proving more fragile than broader ones. In addition, the stability zone shifts towards larger values of the parameter ρ because fluctuations at the lower end of the zone tend to eliminate spatial structure while those at the upper end tend to nucleate new structure. For large enough fluctuation amplitude stable LSs are no longer possible.

We have seen that within their zone of stability the LSs execute a chaotic walk. The properties of this walk are determined by the mobility of the structure, and we have shown by explicit calculation that shorter structures have greater mobility, and hence smaller effective inertia. As a result shorter structures change direction more frequently than longer structures, which are therefore characterized by a broader distribution of step sizes.

Similar behavior is found in two spatial dimensions as well. Figure 11(b) shows several examples of chaotic but

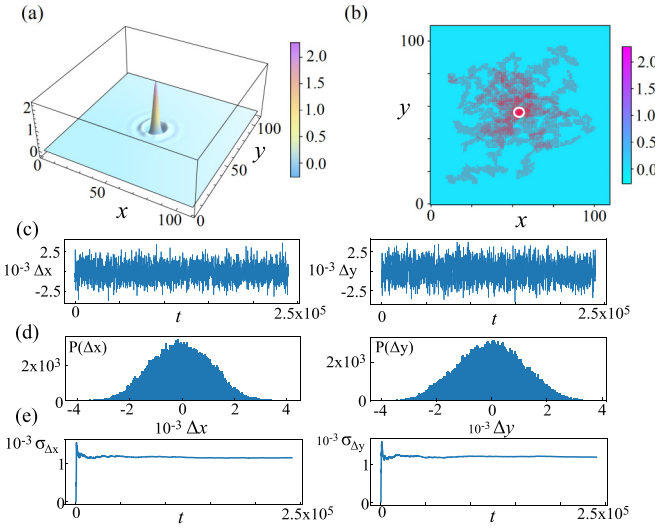

FIG. 11. Chaotic walk in two dimensions of an initially axisymmetric one-bump state (a) for several slightly different initial conditions for Eq. (2) when $b = 2.2$, $\rho = -0.5$, $\gamma = 0.07$, $\eta = 0$ (b). The red dot in (b) shows the location of the structure at $t = 0$. (c) Displacements Δx and Δy of the centroid of a one-bump state in time $dt = 0.01$ as a function of the time t in one realization of the chaotic walk. (d) Associated probability density functions. (e) Evolution of the standard deviations $\sigma_{\Delta x}$, $\sigma_{\Delta y}$ of the resulting displacements.

deterministic walks of a one-bump localized structure [Fig. 11(a)] initially at $(x, y) = (0, 0)$ obtained from different realizations of Eqs. (1) and (2) in two dimensions generated by multiplying u and ψ at each grid point by independent random vectors of magnitude 10^{-3}. No additive noise is included ($\eta = 0$). The figure shows the resulting trajectories in the (x, y) plane while Figs. 11(c) and 11(d) show the statistics of the centroid displacement $(\Delta x, \Delta y)$ in time $dt = 0.01$, defined as in the one-dimensional case, for one of these realizations. These show that the chaotic walk is statistically isotropic with a constant and isotropic standard deviation. Moreover, when averaged over the initial conditions used to generate the different realizations, the distribution of the resulting walks is also isotropic. Thus localized structures in two spatial dimensions undergo similar behavior when subjected to multiplicative deterministic fluctuations as those in one spatial dimension. A detailed study of the properties of these two-dimensional deterministic walks is in progress.

The above results differ fundamentally from those prevailing for Eq. (1) driven stochastically by white noise ($\gamma = 0$). In this case all LSs eventually collapse to either the trivial state $u = 0$ or to a spatially extended state. These two outcomes are separated by an effective Maxwell point that has to be computed as a function of the applied forcing strength η. In fact theoretical interpretations of experimental studies of LSs, in both 1D and 2D [4–6], typically assume that any fluctuations that may be present are of a stochastic nature, and not deterministic. We have shown that a careful examination of the statistical properties of the observed LS dynamics can in principle discriminate between these two possibilities, and provide new insights into the nature of the underlying fluctuations.

Throughout this paper we have adopted periodic boundary conditions. However, it is known that fluctuations in the boundary conditions can in and of themselves lead to unexpected timing jitter in optical signals [33]. A study of the effect of deterministic boundary fluctuations on the dynamics of LSs through their effect on the critical wave number k_c is therefore also of interest, and will be reported on in a future publication.

ACKNOWLEDGMENTS

This work was partially funded by CONICYT-USA Grant No. PII20150011. A.J.A.-S. gratefully acknowledges financial support from Becas CONICYT 2015, Contract No. 21151618.

[1] G. Nicolis and I. Prigogine, *Self-Organization in Nonequilibrium Systems* (J. Wiley & Sons, New York, 1977).
[2] M. C. Cross and P. C. Hohenberg, Rev. Mod. Phys. **65**, 851 (1993).
[3] L. M. Pismen, *Patterns and Interfaces in Dissipative Dynamics*, Springer Series in Synergetics (Springer, Berlin/Heidelberg, 2006).
[4] *Localized States in Physics: Solitons and Patterns*, edited by O. Descalzi, M. Clerc, S. Residori, and G. Assanto (Springer, New York, 2010).
[5] H. G. Purwins, H. U. Bödeker, and Sh. Amiranashvili, Adv. Phys. **59**, 485 (2010).
[6] *Dissipative Solitons: From Optics to Biology and Medicine*, Lecture Notes in Physics 751, edited by N. Akhmediev and A. Ankiewicz (Springer, Heidelberg, 2008).
[7] P. Coullet, Int. J. Bifurcat. Chaos **12**, 2445 (2002).
[8] P. D. Woods and A. R. Champneys, Physica D **129**, 147 (1999).
[9] J. Burke and E. Knobloch, Phys. Rev. E **73**, 056211 (2006).
[10] A. G. Vladimirov, R. Lefever, and M. Tlidi, Phys. Rev. A **84**, 043848 (2011).
[11] D. Turaev, M. Radziunas, and A. G. Vladimirov, Phys. Rev. E **77**, 065201(R) (2008).
[12] K. Staliunas and V. J. Sánchez-Morcillo, Phys. Rev. A **57**, 1454 (1998).
[13] F. Haudin, R. G. Rojas, U. Bortolozzo, M. G. Clerc, and S. Residori, Phys. Rev. Lett. **106**, 063901 (2011).
[14] P. V. Paulau, D. Gomila, T. Ackemann, N. A. Loiko, and W. J. Firth, Phys. Rev. E **78**, 016212 (2008).
[15] A. J. Scroggie, W. J. Firth, and G.-L. Oppo, Phys. Rev. A **80**, 013829 (2009).
[16] M. Tlidi, A. G. Vladimirov, D. Pieroux, and D. Turaev, Phys. Rev. Lett. **103**, 103904 (2009).
[17] A. J. Alvarez-Socorro, M. G. Clerc, and M. Tlidi, Chaos **28**, 053119 (2018).
[18] M. G. Clerc, S. Coulibaly, and D. Laroze, Int. J. Bifurcat. Chaos **19**, 2717 (2009).

[19] B. Schäpers, M. Feldmann, T. Ackemann, and W. Lange, Phys. Rev. Lett. **85**, 748 (2000).
[20] A. Prigent, G. Grégoire, H. Chaté, O. Dauchot, and W. van Saarloos, Phys. Rev. Lett. **89**, 014501 (2002).
[21] D. Barkley and L. S. Tuckerman, Phys. Rev. Lett. **94**, 014502 (2005).
[22] H. Sakaguchi and H. R. Brand, Physica D **97**, 274 (1996).
[23] M. G. Clerc, C. Falcon, and E. Tirapegui, Phys. Rev. E **74**, 011303 (2006).
[24] A. J. Alvarez-Socorro, M. G. Clerc, M. A. Ferré, and E. Knobloch, Phys. Rev. E **99**, 062226 (2019).
[25] W. Horsthemke and R. Lefever, *Noise-induced Transitions* (Springer, Berlin, 1984).
[26] J. Burke and E. Knobloch, Chaos **17**, 037102 (2007).
[27] P. Manneville, *Lecture Notes in Physics*, Vol. 280 (Springer, Berlin, 1994), pp. 319–326.
[28] Y. Kuramoto, Prog. Theor. Phys. Suppl. **64**, 346 (1978).
[29] S. Toh, J. Phys. Soc. Jpn. **56**, 949 (1987).
[30] S. M. Houghton and E. Knobloch, Phys. Rev. E **84**, 016204 (2011).
[31] C. Cartes, J. Cisternas, O. Descalzi, and H. R. Brand, Phys. Rev. Lett. **109**, 178303 (2012).
[32] C. Martel, E. Knobloch, and J. M. Vega, Physica D **137**, 94 (2000).
[33] H. Haus and A. Mecozzi, IEEE J. Quant. Electron. **29**, 983 (1993).